ADVANCED FUNCTIONAL MATERIALS
www.afm-journal.de

Coupling of Infrared Active Colloidal Quantum Dots and Amorphous Selenium for Fast and Sensitive Photodetection

Håvard Mølnås, Atreyo Mukherjee, Haripriya Kannan, Zhihang Han, Vikash K. Ravi, Shlok J. Paul, Abdul K. Rumaiz, Wei Zhao, Amir H. Goldan, and Ayaskanta Sahu**

Colloidal quantum dot (CQD) based infrared (IR) photodetectors offer facile wavelength tunability in the IR and low-cost fabrication. However, owing to their large surface areas, CQDs intrinsically have significant surface traps critically affecting the speed of CQD photodetectors, typically mediated through tedious surface passivation efforts. In this report, an alternative strategy involving coupling of near-IR photoactive lead sulfide CQDs with a thermally evaporated amorphous selenium (a-Se) hole transport layer is proposed. By separating the detector into a photon absorbing CQD region and a charge transport a-Se region, the study takes advantage of the extremely low noise, predominantly hole-only transport process in a-Se. A high 3 dB bandwidth of 2.5 MHz and a competitive specific detectivity of 2.5×10^{11} Jones at room temperature are demonstrated at 980 nm. This report serves as a first demonstration of strong coupling between an IR active CQD absorber and a-Se, which paves the path to obtain fast and highly photoresponsive IR photodetection in the future.

1. Introduction

Infrared (IR) photodetection is gaining momentum as areas of utilization are expanded beyond the traditional high-end avenues such as astronomy and military surveillance to agriculture, industry, autonomous vehicles, and personal devices.[1–4] Fabricating fast sensors operating at specific desired wavelengths of the energetically wide IR spectrum (0.78–1000 µm, ref. ISO 20473)[5] ideally requires high mobility and low noise semiconductor absorbers with significant band gap tunability, which current state-of-the-art bulk materials do not offer without overcoming significant technological and economic hurdles.[6]

Alternatively, semiconductor colloidal quantum dots (CQDs) offer impressive band gap tunability through size and surface modification. These nanometer-sized particles can be solution-synthesized at low temperatures from simple precursors at relatively low cost and allow for facile deposition over a wide range of substrates.[7–9] Therefore, CQDs enable easy optoelectronic access to a broad range of the electromagnetic spectrum with a limited portfolio of semiconductor chemistries. For example, with its large (36 nm) Bohr diameter, lead sulfide (PbS) CQDs can be tuned to have a band gap ranging from the near infrared (NIR) to the extended short-wave infrared (E-SWIR) (800-2200 nm) solely by varying the size of the particles (2.5–11.5 nm).[10–12] Owing to these impressive optical properties, CQDs are currently showing promise in a wide range of applications ranging from displays and lighting,[13,14] optical sensing and imaging,[3] lasing,[15] solar energy harvesting,[16] bioimaging and medicine,[17] and quantum light generation.[8] In this study, we focus on the potential of CQDs in IR photodetectors, some of the issues faced, and present a potential strategy to overcome these hurdles towards commercial adoption.

The sensitivity of a photodetector is determined by its ability to deliver a signal that is high enough with respect to the noise current to yield a competitive signal-to-noise ratio. However, solution-processed CQD detector structures are plagued with high dark currents. Due to their small size, CQDs have a large surface-to-volume ratio compared to bulk particles, which makes them prone to having a significant number of trap states typically caused by charged metal cation rich surfaces.[18] Large trap densities with energy near a band edge ("shallow traps")

H. Mølnås, H. Kannan, V. K. Ravi, S. J. Paul, A. Sahu
Department of Chemical and Biomolecular Engineering
Tandon School of Engineering
New York University
Brooklyn, NY 11201, USA
E-mail: asahu@nyu.edu

A. Mukherjee, Z. Han
Department of Electrical Engineering
College of Engineering and Applied Sciences
Stony Brook University
Stony Brook, NY 11794, USA

A. K. Rumaiz
National Synchrotron Light Source II
Brookhaven National Laboratory
Upton, NY 11973, USA

W. Zhao, A. H. Goldan
Department of Radiology
School of Medicine
Stony Brook University
Stony Brook, NY 11794, USA
E-mail: amg4017@med.cornell.edu

A. H. Goldan
Department of Radiology, Weill Cornell Medical College
Cornell University
New York, NY 10065, USA

The ORCID identification number(s) for the author(s) of this article can be found under https://doi.org/10.1002/adfm.202315304

DOI: 10.1002/adfm.202315304

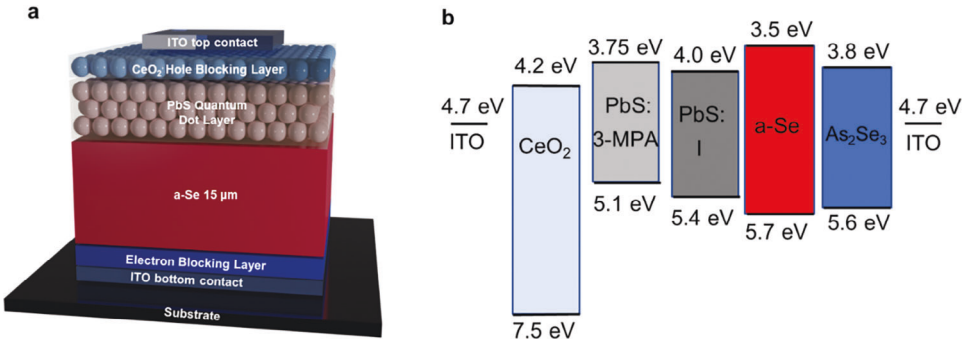

Figure 1. a) Vertical photodetector architecture coupling NIR active PbS CQDs with a-Se. b) Band diagram for the vertical photodetector. Absolute band edge energies were obtained from Kannan et al.[33] (CeO_2, a-Se, As_2Se_3), Brown et al.[34] (PbS:3-MPA), and Wang et al.[35] (PbS:I, ITO).

significantly lower the speed of the CQD photodetector, and can be detrimental for sensors for (tele)communications or other high-frequency environments. This issue is exacerbated especially in the IR owing to the low bandgap of the absorber leading to higher dark currents and noise at room temperature. Moreover, most large-area CQD fabrication techniques lead to incomplete coverage of the substrate, undesirable pinholes, and cracks (thin CQD films often contain pinholes, whereas thicker films are likely to exhibit cracking).[16] This reduces film density, consequently lowering absorption per unit length, while simultaneously creating potential electrical shorts through the film and lowering electrical conductivity compared to a continuous film. Generally, even for the most highly-studied IR CQD system – PbS, the most sensitive photodetectors show a slow time response,[19] while the fastest photodetectors typically sacrifice some photosensitivity.[20,21] Table S1 (Supporting Information) compares sensitivity and time response for PbS CQD photodiodes at ≈1000 nm reported in literature.

A common strategy to passivate traps in CQDs is through careful surface ligand engineering.[4,22] An alternative strategy to tedious and inconsistent surface passivation of CQDs is to separate absorption and charge extraction – a well-known technique from early dye-sensitized solar cell technology[23] – which for CQD photodetection has been shown to reduce noise and improve photoresponse.[24–26] In this regard, we propose using amorphous selenium (a-Se) as a solid-state hole transport layer (HTL) for charge extraction in CQD photodetectors.

a-Se can be easily deposited uniformly over large areas through thermal evaporation due to its low melting point and high vapor pressure, forming up to 1000 µm thick layers.[27] Owing to its wide band gap (~2.2 eV) and high resistivity, a-Se demonstrates intrinsically low dark currents and low thermal noise at low bias, as well as ultra-low leakage current (~30 pA cm^{-2}) even at high electric fields.[28] Historically, a-Se has been extensively explored for X-ray detection to amplify the signal and reduce noise for low dose applications.[29,30] The avalanche effect in a-Se is unique, wherein it exhibits low-noise single carrier hole impact ionization, effectively amplifying signals at electric fields above ≈70 V $µm^{-1}$. Thus, avalanche a-Se is currently being explored for utilization in commercial X-ray detectors.[27,31]

Unfortunately, owing to its large bandgap, a-Se cannot be operated in the IR spectral region and thus cannot be used as a standalone IR detector. Another major issue working with a-Se is that it is highly sensitive to temperatures above its glass transition temperature (50 °C),[29] and also demonstrates incompatibility with many traditional fabrication and deposition processes that use organic solvents, causing crystallization.[32] Our approach focuses on ameliorating the issues with typical CQD-based detectors and a-Se detectors by coupling these together and exploiting the best features of both technologies to deliver a highly efficient IR detector. The solution-processed IR CQD photon conversion layer can be successfully deposited over a thick (15 µm, required to enable sufficient avalanche gain) a-Se layer at room temperature, without inducing any surface or bulk crystallization, rendering an operable device by avoiding electrical shorts even in the presence of micro-cracks and voids in the CQD layer (**Figure 1a**). By separating the detector into a photon-absorbing CQD region and a charge transport a-Se region, we can now take advantage of the low-noise, predominantly hole-only transport process in a-Se.

Our group has previously shown successful coupling of a-Se and solution-deposited CQDs.[28,33] A ceria (CeO_2) CQD hole blocking layer deposited between the a-Se and the positive electrode reduced the dark current density significantly under high electric fields sufficient to benefit from the avalanche effect. At the onset of avalanche, an ultra-low dark current of 30 pA cm^{-2} was reported – outperforming all other solid-state avalanche sensors at room temperature.[28] Building on these results, a cadmium selenide (CdSe) CQD absorber layer was integrated into the device structure, spatially separating the photon absorption and carrier extraction. High specific detectivity, D^*, of 0.5 – 5 × 10^{12} Jones and fast 3 dB bandwidth, ≈22 MHz, in the visible range (405 – 656 nm) was achieved.[33]

While visible photodetection using CQDs is scientifically interesting, we believe that a higher degree of technological disruption could occur in the IR range utilizing this heterostructure. Therefore, in this report, we fabricated vertical IR photodetectors coupling the most well-studied NIR active CQD system, PbS CQDs, with a-Se and appropriate carrier blocking layers. We report a high 3 dB bandwidth of 2.5 MHz and a D^* of 2.5 × 10^{11} Jones, competitive with state-of-the-art fast and photoresponsive photodiodes at 980 nm.[20,21] The avalanche effect in a-Se unfortunately could not be explored owing to the mismatch in energy band levels between PbS and a-Se leading to Joule heating and crystallization of a-Se at high electric fields. We believe that future improvements in performance could be achieved through optimized band edge energy alignment between the IR CQDs

absorber layer and the a-Se, as well as more streamlined device fabrication preventing crystallization of a-Se. Nevertheless, we have demonstrated for the first time a proof of concept for integrating IR active CQDs with a-Se in a vertical device structure, which opens the door to IR active photodetectors benefiting from the avalanche effect in the future. Our results pave the path for the use of a-Se as a reliable, stable, wide-bandgap charge transport layer, which can now be coupled to existing and emerging CQDs to obtain optimal EQEs while maintaining an ultra-low dark current density.

2. Results and Discussion

2.1. PbS CQD a-Se Photodetector Architecture

NIR active PbS CQDs with first excitonic peak ≈1000 nm were synthesized as described in the Experimental section. Briefly, two different variations of PbS CQDs were synthesized via an adaptation[36] of the traditional Hines route[37] based on a lead oleate precursor forming oleate capped PbS (PbS:OA), and a room temperature direct route[35] based on a lead (II) iodide-N,N-dimethylformamide complex precursor forming iodide capped PbS (PbS:I). These two sets of NIR PbS CQDs were used to enable a thicker active layer and improve the pn-junction. XRD patterns, solution absorbance spectra, and TEM images of the CQDs are shown in Section S2 (Supporting Information).

The PbS CQDs were integrated through spin coating into a vertical photodetector structure with CeO_2 CQDs and thermally evaporated a-Se serving as electron and hole transport layers, respectively, and with indium tin oxide (ITO) top and bottom contacts, as illustrated in Figure 1a. Solution deposition of CQDs on top of a-Se required careful consideration of solvents and techniques used, as discussed in detail in Section S3 (Supporting Information), in order to avoid irreversible crystallization of Se.

Crystalline Se exists as monoclinic or hexagonal allotropes, hexagonal Se (c-Se) being the most thermodynamically stable with a work function of 5.9 eV, absorption coefficient above 10^4 cm^{-1} and a bandgap of ≈1.85 eV.[38] For comparison, a-Se has a higher band gap (≈2.2 eV) and a lower carrier mobility than c-Se, due to the lack of a long-range ordered structure. Additionally, having the unique capability of avalanche gain, a-Se is more suitable for detection, while c-Se is more suitable as a high band-gap absorber for a tandem silicon solar cell.

Avoiding initial crystallization of a-Se we hypothesized that, at high electric fields, the avalanche effect of a-Se[30] would contribute additional electron-hole pairs and thus amplify the photoresponse while keeping noise levels low due to the single carrier impact ionization and non-Markovian branching processes for hot holes.[28] The band edge energy alignment is shown in Figure 1b), based on band edge energies from literature.[33–35]

2.2. Key Photoresponse Parameters

In a photodetector, key processes taking place are photon absorption and efficient transport of photoexcited charge carriers to the contacts. Both of these processes are affected by the thickness of the photoactive layer, although in opposite directions, requiring careful balancing of absorption and charge transport for optimized performance. Traditionally, the performance of photodetectors is compared using the specific detectivity, $D^*(\lambda)$, calculated through Equation (1), where $R(\lambda)$ is the responsivity as a function of wavelength, Equation (2), closely related to the external quantum efficiency (EQE), Equation (3):[11]

$$D^*(\lambda) = \frac{R(\lambda)\sqrt{A}}{\sqrt{I_n^2}} \tag{1}$$

$$R(\lambda) = \frac{i_{ph}(\lambda)}{P_{in}(\lambda)} \tag{2}$$

$$EQE(\lambda) = R(\lambda)\frac{hc}{q\lambda} \tag{3}$$

A is the device area, I_n is the noise current spectral density, $i_{ph}(\lambda)$ is the wavelength-dependent photocurrent, $P_{in}(\lambda)$ is the input power to the sample at each wavelength of interest, h is Planck's constant, c is the speed of light, q is elementary charge and λ is the wavelength of the electromagnetic radiation. D^* as high as 7.0×10^{13} Jones has been reported for PbS CQD photodiodes in the NIR.[19]

The temporal response of the photodetector can be characterized in terms of the 3 dB bandwidth, also known as the cut-off frequency, f_{3dB}.[11] This parameter can be determined experimentally as the light modulation frequency where the photocurrent drops below $\frac{1}{\sqrt{2}} = \approx 70.7\%$ of the peak value, or calculated based on response time, τ, according to Equation (4):

$$f_{3dB} = \frac{1}{2\pi\tau} \tag{4}$$

Response times as low as 7–10 ns have been reported for PbS CQD photodiodes,[20,21] yielding calculated 3 dB bandwidths in the MHz range, although a recent study utilizing a two-pulse coincident photoresponse technique has indicated that the intrinsic response time of the PbS CQDs could be lower than 1 ns.[39] Because of the trade-off between absorption and charge transport in a CQD based photodetector, it is useful not only to compare D^*, but also the D^* x 3 dB bandwidth product.[33,40] Current state-of-the-art fast and sensitive PbS CQD photodetectors have D^* x 3 dB bandwidth products on the order of 10^{19}–10^{20} Jones x Hz.[20,21,41]

2.3. PbS CQD – a-Se Vertical Photodetector Performance

Vertical photodetectors coupling PbS CQDs with a-Se were fabricated as described in the Experimental section and visualized in Figure 1 and Figure S7 (Supporting Information). **Figures 2 and 3** show photoresponse, noise current spectral density and frequency response for our best performing device at 5 and 10 V μm^{-1} electric fields. Application of electric fields larger than 10 V μm^{-1} led to excessive noise, likely due to a-Se crystallization, thus masking the signal. Additional photoresponse data are shown in Figures S8–S10 (Supporting Information).

Responsivity and on/off current density ratio, J_{light}/J_{dark}, are reported in Figure 2a,b. It can be observed that the responsivity

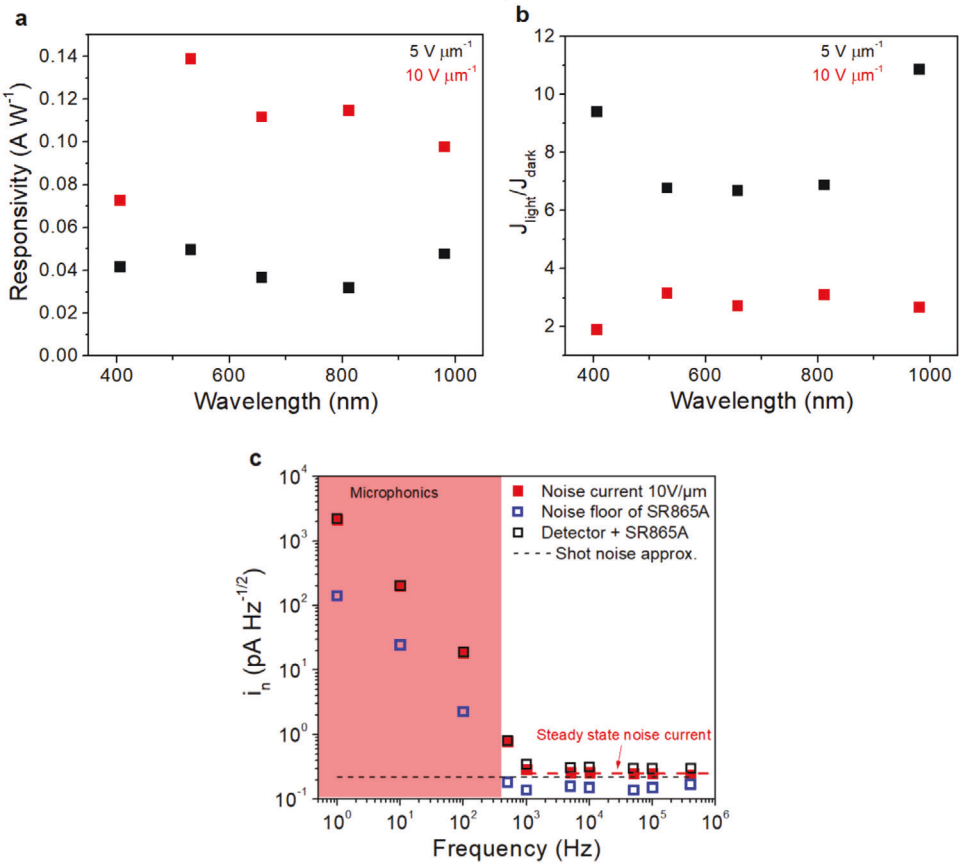

Figure 2. a) Responsivity and b) J_{light}/J_{dark} for a PbS CQD a-Se photodetector at 5 V µm^{-1} (black squares) and 10 V µm^{-1} (red squares). Responsivity was improved under higher electric field, while J_{light}/J_{dark} decreased. c) Noise current spectral density with shot noise approximation, total noise and noise floor approximations indicated as black dashed line, black open squares, and blue open squares, respectively. Microphonics interfere with low-frequency measurements. Stabilized noise current spectral density at 10 V µm^{-1} was determined to 0.251 pA Hz$^{-1/2}$, as shown as red dashed line.

improves with increasing electric field, as expected due to the increased driving force for charge carrier extraction, while the J_{light}/J_{dark} decreases with increasing electric field, as the dark current density increased more than the light current density. Compared to other PbS CQD photodiodes operating at ≈1000 nm reported in literature, presented in Table S1 (Supporting Information), our device performs about one order of magnitude poorer in terms of responsivity at 980 nm.[42] This could be due to carrier recombination at the transport layer interfaces or incomplete charge extraction in our devices. The average dark current density was ≈69 nA cm^{-2} at 5 V µm^{-1} and ≈522 nA cm^{-2} at 10 V µm^{-1}, which is comparable to literature reports for PbS CQD photodiodes with low applied bias.[21,43]

Figure 2c shows the noise current spectral density at 10 V µm^{-1}, which follows a decreasing trend below 1 kHz, potentially due to microphonics in the SR865A lock-in amplifier,[33] and stabilizes around the shot noise limit (black dashed curve), $i_{shot} = \sqrt{2qGI_{dark}}$, above 1 kHz. q is the electron charge, G is gain and I_{dark} is the dark current. The noise current spectral density at 5 V µm^{-1} was not measured but can be approximated to 0.084 pA Hz$^{-1/2}$ above 1 kHz based on the shot noise limit with no gain (G = 1). The specific detectivity at 10 V µm^{-1} at 980 nm can be determined to 2.5 × 10^{11} Jones based on the measured responsivity and stabilized noise current spectral density in accordance with Equation (1), as reported in Figure S9 (Supporting Information). This is comparable to state-of-the-art fast and sensitive PbS CQD photodiodes,[20,21] however is several orders of magnitude behind the most photoresponsive PbS CQD photodiodes at 1000 nm.[19] In comparison, a commercial bulk indium gallium arsenide (InGaAs) photodiode has a D^* of 4.0 – 5.0 × 10^{12} Jones at 1000 nm.[19,49]

The 3 dB bandwidth at 5 V µm^{-1} was determined to 2.5 MHz, as shown in **Figure 3a**, corresponding to a response time of ≈64 ns in accordance with Equation (4). This is only about one order of magnitude slower than state-of-the-art PbS CQD photodiodes.[20,21] The 3 dB bandwidth of a commercial bulk InGaAs photodiode can reach the GHz range. We were not able to determine the 3 dB bandwidth at 10 V µm^{-1} due to unstable readings caused by leaky pixels, indicating pixel break-down.

Figure 3b shows the D^* x 3 dB bandwidth product for our best-performing device at 5 V µm^{-1} compared against PbS CQD photodiodes at ≈1000 nm reported in the literature. Our device is one of the fastest vertical PbS CQD devices reported at ≈1000 nm, however it performs a few orders of magnitude lower in terms of D^*. Therefore, the D^* x 3 dB bandwidth product for our device is on the order of 10^{18} Jones x Hz, whereas the highest performing

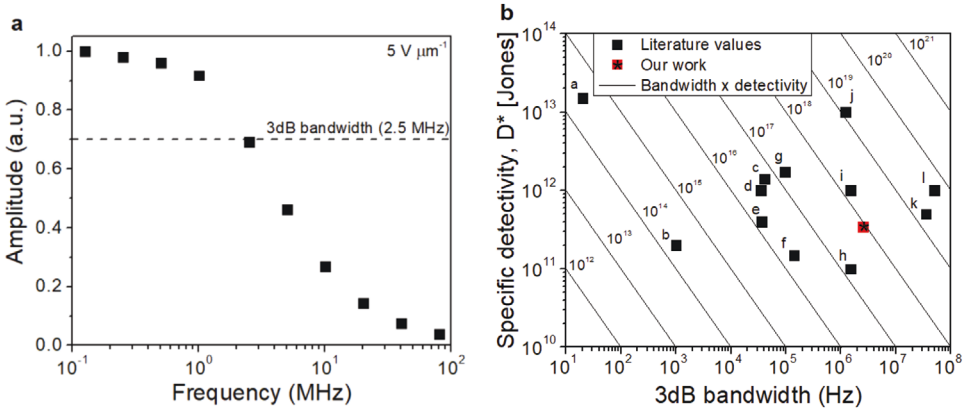

Figure 3. a) 3 dB bandwidth and b) D^* x 3 dB bandwidth product for our best PbS CQD a-Se device at 5 V μm^{-1} (red square) compared with PbS CQD photodiodes at ≈1000 nm reported in literature (black squares): a,[19] b,[42] c,[44] d,[45] e,[43] f,[40] g,[46] h,[47] i,[48] j,[41] k,[21] l.[20] Solid diagonal lines represent D^* x 3 dB bandwidth products. D^* was calculated using shot noise limit at high frequency assuming $G = 1$.

devices achieve a D^* x 3 dB bandwidth product on the order of 10^{19}–10^{20} Jones x Hz.[20,21,41]

It is important to note that our results were achieved without benefiting from the avalanche effect in a-Se, which could potentially provide avalanche gain and improve our performance by orders of magnitude.[28,50] Currently, electric fields in excess of 10 V μm^{-1} could not be applied for our devices without drowning the photoresponse signal in noise, likely due to recombination at the CQD a-Se interface, possibly causing Joule heating and crystallization of the a-Se. The uniformity of the blocking layers could also be an issue, causing current leakage and increased noise at high bias. Nevertheless, photoluminescence (PL) measurements for as-synthesized PbS:OA CQDs on glass and on a-Se/glass, shown in Figure S11 (Supporting Information), demonstrate nearly complete (≈90%) quenching of PL for PbS CQDs on a-Se/glass compared to PbS CQDs on glass. This could suggest charge transfer from the PbS CQDs to a-Se, or alternatively recombination at the PbS/a-Se interface or due to shallow CQD traps. Enhancing the quality of the interface as well as CQD passivation is thus expected to improve the photoresponse.

More importantly, we believe that our D^* x 3 dB bandwidth product can be improved through attaining a type-II band edge energy alignment between the CQD active layer and the a-Se. Bulović and Bawendi et al.[34,51] have shown that the band edge energies of PbS CQDs can be tuned over a range of almost 1 eV through ligand engineering. However, few or no ligands are theoretically capable of shifting the valence band (VB) energy of PbS CQDs below the VB energy of a-Se, −5.7 eV, resulting in a less than ideal band alignment even in the best possible scenario (Figure 1b). Ideally, a type-II alignment between the valence and conduction bands of PbS CQD and a-Se would provide a sufficient driving force for hole transport from the CQD active layer into the a-Se, while blocking electrons from flowing in the same direction. We hypothesized that the application of a large external bias would bend the energy bands and thus more ideal alignment would be achieved, although based on the photoresponse of vertical PbS CQD photodetectors comparing different HTLs, shown in Figure S10 (Supporting Information), vertical devices with molybdenum trioxide (MoO_3) and Spiro-OMeTAD HTLs outperform devices with a-Se even at biases up to 5 V.

The sum of these observations leads us to conclude that coupling a-Se with a different IR active CQD system than PbS would be preferred to benefit to a higher extent from a-Se in this heterostructure. Though, other popular and heavily researched IR active CQD systems also have less than ideal theoretical band energy alignment with a-Se at zero bias (NIR Ag_2Se CQDs have a VB energy of ≈5 eV,[24,52] PbSe CQDs have VB at ≈5.5 eV,[53] and HgTe CQDs have VB at ≈5 eV.[54,55]). Therefore, alternative IR active CQD semiconductors with more ideal band alignment with a-Se would be beneficial to extract the full potential of this approach. Nevertheless, through coupling PbS CQDs with a-Se in this study, as well as our earlier work coupling CdSe CQDs with a-Se,[33] we have demonstrated the potential of using a-Se as a promising charge extraction layer in CQD-photodetectors to achieve high speed and competitive photoresponse.

3. Conclusion

For CQD-based IR photodetectors to reach their full potential, the tradeoff between photoresponse, maximizing photon absorption, and 3 dB bandwidth, requiring fast charge transfer, must be lifted. While much work has gone into passivation of CQD surfaces to remove trap states, we here propose an alternative strategy that involves coupling an IR PbS CQD photoconversion layer with an a-Se layer acting as a wide bandgap charge transport layer. The thick (15 μm) a-Se charge transport layer enables optimal device performance even in the presence of macroscopic cracks that would otherwise short circuit the detector when the common metal electrode is directly connected to the CQD film. This enables the fabrication of reliable devices with ultra-low leakage and high quantum efficiencies even in the presence of micro and nano-scale voids. Our vertical architecture NIR PbS CQD a-Se photodetectors demonstrate a high 3 dB bandwidth of 2.5 MHz, yielding a D^* x bandwidth product of 8.6×10^{17} Jones x Hz at 980 nm and 5 V μm^{-1}, without benefiting from the avalanche effect inherent to a-Se. A competitive D^* of 2.5×10^{11} Jones was measured at 980 nm and 10 V μm^{-1}. Through optimized band energy level alignment between the CQDs and a-Se, as well as access to avalanche gain, we believe that the IR photodetector performance can be improved further. The findings in this work

provide a simple method to improve the efficiency of CQD-based photodetectors and serve as a first demonstration of integrating IR active CQDs with a-Se in a vertical photodiode structure. This opens the door to future IR active photodetectors benefiting from the avalanche effect.

4. Experimental Section

Chemicals: Lead (II) acetate trihydrate ($Pb(OAc)_2 \cdot 3\ H_2O$, puriss. 99.5-102.0%) oleic acid (OA, 70%, technical grade), 1-octadecene (ODE, 90%, technical grade), oleylamine (OlAm, technical grade, 70%), bis(trimethylsilyl)sulfide ($(TMS)_2S$, synthesis grade), lead (II) iodide (PbI_2, 99.999% trace metal basis), *N*,*N*-dimethylformamide (DMF, anhydrous, 99.8%), *N*,*N*'-diphenylthiourea ($((C_6H_5NH)_2CS$, 98%), butylamine ($C_4H_9NH_2$, 99.5%), toluene ($C_6H_5CH_3$, anhydrous, 99.8%), hexane (C_6H_{14}, anhydrous, 95%), ethyl alcohol (CH_3CH_2OH, anhydrous, ≥99.5%), octane (C_8H_{18}, anhydrous, ≥99%), 3-mercaptopropionic acid (3-MPA, ≥99%), cerium (III) nitrate hexahydrate ($Ce(NO_3)_3 \cdot 6\ H_2O$, 99.99% trace metal basis) were purchased from Sigma-Aldrich. Acetone (C_3H_6O, extra dry, 99.8%) was purchased from Acros Organics. n-octane (C_8H_{18}, synthesis grade, >99%) was purchased from Merck KGaA. Ethanol (reagent grade), methanol (reagent grade), isopropanol (reagent grade), acetone (reagent grade), and hexane (reagent grade) were purchased from Greenfield Global. All chemicals were used as received without further purification.

PbS CQD Synthesis: PbS CQDs with long oleate (OA) ligands were synthesized based on a route[36] adapted from the Hines method.[37] 764.8 mg lead (II) acetate trihydrate, 2.25 mL OA, and 12.7 mL ODE were loaded into a 50 mL three-neck flask and degassed on a Schlenk line at 110 °C for 1 hour. The solution turned clear during this process, forming lead oleate precursor. In the meantime, sulfur (S) precursor was prepared in a nitrogen (N_2)-filled glovebox. 5 mL degassed ODE was used to dilute 0.210 mL of $(TMS)_2S$ in a syringe. After degassing, the lead oleate solution was heated to 120 °C under N_2-atmosphere, and the S precursor was injected rapidly. The heating mantle was removed immediately before injection, to allow for natural cooling of the products after injection/nucleation. The PbS:OA CQDs were precipitated with ethanol, and cleaned twice using hexane and ethanol in a N_2-filled glovebox.

PbS CQDs with iodide ligands were synthesized in a N_2-filled glovebox in a direct synthesis procedure first reported by Wang et al.[35] 1843 mg PbI_2 and 237 mg *N*,*N*'-diphenylthiourea (4:1 Pb:S molar ratio) were dissolved in 4.5 mL DMF under stirring at room temperature. 0.5 mL butylamine was injected rapidly, swiftly forming a black PbS CQD dispersion. The CQDs were grown at room temperature for 1 min, before transferring the dispersion to two Falcon tubes and adding 12 mL anhydrous toluene to each. Upon centrifugation, the PbS:I CQDs precipitated and the supernatant was discarded, before the CQDs were dried under vacuum for 30 min.

CeO_2 CQD Synthesis: ≈5.3 nm CeO_2 CQDs were synthesized on a Schlenk line following a route adapted from Runnerstrom et al.,[56] as reported previously.[28] Briefly, 2 mmol/2.605 g cerium (III) nitrate hexahydrate was decomposed in 24 mL OlAm and 15 mL ODE (in a three neck flask) at 250 °C. The CQDs were grown for 2 hours and cooled naturally, before precipitation and further cleaning with ethanol and hexane under ambient conditions. OA treatment was performed to provide additional colloidal stability.

Deposition of Amorphous Selenium (a-Se): 15 µm a-Se was deposited in accordance with previous reports.[28,33] Briefly, stabilized vitreous Se pellets were thermally evaporated through a shadow mask onto 1 inch x 1 inch borofloat glass substrates coated with 75 nm indium tin oxide (ITO) serving as a bottom contact and a 2 µm inorganic electron blocking layer. Substrates were stored under vacuum in the dark until needed.

Device Fabrication: A single layer of PbS:I was deposited through spin coating (static dispense, 2000 rpm, 45 sec) from a 500 mg mL^{-1} CQD in DMF solution onto the a-Se substrates and dried under vacuum for 10 min. Subsequently, ten layers of PbS:3-MPA were deposited on top of the PbS:I layer through sequential spin coating of 50 mg mL^{-1} CQD in octane solution (dynamic dispense, 2500 rpm, 10 sec), ligand exchange from OA to 3-MPA through spin coating of 1 vol% 3-MPA in acetone (dynamic dispense, 2500 rpm, 10 sec) and two times rinse through spin coating neat acetone (dynamic dispense, 2500 rpm, 10 sec). Finally, a single layer (≈50 nm)[33] of CeO_2:3-MPA was deposited on top of the PbS layers through spin coating of 30 mg mL^{-1} CQD in 9:1 hexane:octane solution (dynamic dispense, 2000 rpm, 45 sec), ligand exchange from OlAm to 3-MPA through spin coating 1 vol% 3-MPA in acetone (dynamic dispense, 2000 rpm, 45 sec) followed by rinse through spin coating neat acetone (dynamic dispense, 2000 rpm, 10 sec). As top contact, 50 nm ITO was deposited through a shadow mask via room temperature electron beam deposition by an external company (Hionix Inc), completing the vertical devices with area ≈0.32 cm^2.

For devices with MoO_3 HTL, 15 nm MoO_3 was deposited by thermal deposition under N_2 atmosphere using a mask to define the device area. For devices with Spiro-OMeTAD HTL, a single layer of Spiro-OMeTAD was deposited under N_2 atmosphere as reported in literature.[57] Spiro-OMeTAD dissolved in chlorobenzene (100 mg mL^{-1}) and doped with 20 µL bis(trifluoromethylsulfonyl)imide lithium salt (Li-TFSI) in acetonitrile (517 mg mL^{-1}), 8 µL tris(2-(1H-pyrazol-1-yl)−4-tertbutylpyridine)-cobalt(III) tris(bis(trifluoromethylsulfonyl)imide) (FK209) in acetonitrile (376 mg mL^{-1}) and 36 µL 4-tert-butylpyridine was spin coated at 3500 rpm for 40 sec on top of the PbS CQD layers. The samples were aged in a N_2-filled glovebox at ppm oxygen (O_2) levels for 12 hours before exposure to ambient conditions.

UV–vis–NIR Spectroscopy: Absorbance spectra were collected using a CARY 5000 UV–vis–NIR spectrometer. Specifically, for solution absorbance the CQDs were dispersed at low concentration in toluene (PbS:OA) or DMF (PbS:I) and the solvent background spectra was subtracted. For film absorbance, 50 mg mL^{-1} PbS:OA CQD in octane was spin coated onto sonicated (10 min in acetone, isopropyl alcohol, methanol) 1 × 1 inch glass substrates and ligand exchanged from OA to 3-MPA as described above, while PbS:I was spin coated from 500 mg mL^{-1} in DMF without further ligand exchange. The spectrum of the clean glass substrate was subtracted as background.

Photoluminescence (PL): PL spectra were collected using a Horiba Quantamaster Fluorometer. The thin film samples were excited at 800 nm (5 nm bandwidth) using a 75 W Xenon arc lamp filtered by a double monochromator, and the emission detected, after filtering with a single monochromator, using a liquid N_2-cooled InGaAs detector. Sample preparation consisted of drop casting 46 mg mL^{-1} PbS:OA CQDs in hexane onto a 1×1 cm clean glass or a-Se/glass substrate. Absorbance measurements were taken of the same samples for normalization of emission with respect to CQD concentration.

X-Ray Diffraction (XRD): Wide angle XRD spectra from CQDs drop cast on glass substrates were collected using a Bruker AXS D8 Discover GADDS XRD micro-diffractometer equipped with a Cu-Kα source (λ = 1.5405 Å).

Transmission Electron Microscopy (TEM): A Titan Themis 200 S TEM was used to acquire TEM images of the CQDs. Samples were prepared by drop casting sonicated, dilute concentrations of CQDs dispersed in ethanol (PbS:I) and hexane (PbS:OA) onto lacey carbon coated copper grids. Particle sizes were analyzed using ImageJ software.

Dark- and Photocurrent Measurements: The vertical CQD a-Se photodetectors were mounted in a light tight, shielded, grounded metal box. Illuminating the sample through the transparent top ITO contact, Mightex's PLS- series precision LED light sources at 405, 530, 656, 810, and 980 nm were used to provide high-intensity and uniform illumination. The irradiance was calibrated using a Thorlabs PM400 optical power and energy meter placed at the position of the CQD photodiode. The top ITO electrode was positively biased using a CAEN N1471A programmable high voltage (HV) power supply to provide electric fields of 5 and 10 V μm^{-1}. Prior to light exposure, the target HV bias was held for several seconds. After each measurement, the HV bias was ramped down to 0 V and the light tight box was opened to depolarize the sample. A Keithley 6514 electrometer was used to measure the voltage dependent dark/photo current (*I*–*V*) characteristics, and the signal current from a single LED pulse was

used to evaluate the effective quantum efficiency at each applied electric field. The dark current was subtracted from each measured signal current to mitigate offset in the photogenerated charge. All measurements were performed in ambient at room temperature (295 K).

3 dB Bandwidth: A 405 nm picosecond PicoQuant Laser source was utilized to measure the 3 dB bandwidth of the photodetectors, defined as the frequency where the normalized photocurrent is ≈0.7 times that of its steady state value. For each measurement, the frequency of the laser was doubled, simultaneously doubling the power contained in each laser pulse. A Keithley 6514 electrometer was used to measure the current, and the results were normalized by accounting for the doubling in power.

Noise Current Spectral Density: Noise current spectral density was measured using a Stanford Research Systems (SRS) SR865A lock-in amplifier operating in current mode. Measurements were conducted in the dark, isolating the samples in a light-tight box. Additionally, a Faraday shield was constructed using Al foil to prevent interference from microphonics, however the contribution from microphonics was still considered significant below 1 kHz.

Supporting Information

Supporting Information is available from the Wiley Online Library or from the author.

Acknowledgements

This study was funded by the Young Faculty Award program of the Defense Advanced Research Projects Agency (DARPA) under the grant # D21AP10118. Research was sponsored by the Army Research Office and was accomplished under Grant number W911NF-21-1-0056. The views and conclusions contained in this document are those of the authors and should not be interpreted as representing the official policies, either expressed or implied, of the Army Research Office, Department of Defense or the U.S. Government. The U.S. Government is authorized to reproduce and distribute reprints for Government purposes notwithstanding any copyright notation herein. The work was also supported by the National Science Foundation under award ECCS-2048397. The work by the author H.K. was partially supported by the Schlumberger Foundation Faculty for the Future Program. The authors also gratefully acknowledge support for instrument use, scientific and technical assistance from the NYU Shared Instrumentation Facility through the Materials Research Science and Engineering Center (MRSEC) and MRI programs of the National Science Foundation under Award numbers DMR-1420073 and DMR-0923251 and the Imaging and Surface Science Facilities of the Advanced Science Research Center at the Graduate Center of CUNY. The authors gratefully acknowledge Prof. Eray S. Aydil for use of PL instrumentation, Prof. André D. Taylor for use of thermal evaporator for MoO_3 deposition, Dr. Min-Woo Kim and Prof. Stephanie S. Lee for assistance with Spiro-OMeTAD deposition, and Dr. Steven L. Farrell for assistance visualizing the device structure.

Conflict of Interest

The authors declare the following competing financial interest(s): A.H.G., A.S., W.Z., A.M., and H.K. have filed a provisional patent application 63/270,773 based on the results of this manuscript.

Data Availability Statement

The data that support the findings of this study are available from the corresponding author upon reasonable request.

Keywords

amorphous selenium, bandwidth, colloidal quantum dot, infrared photodetector, lead sulfide

Received: December 1, 2023
Revised: March 18, 2024
Published online:

[1] C. L. Tan, H. Mohseni, *Nanophotonics* **2018**, *7*, 169.
[2] H. Lu, G. M. Carroll, N. R. Neale, M. C. Beard, *ACS Nano* **2019**, *13*, 939.
[3] T. Nakotte, S. G. Munyan, J. W. Murphy, S. A. Hawks, S. Kang, J. Han, A. M. Hiszpanski, *J. Mater. Chem. C* **2022**, *10*, 790.
[4] W. Gong, P. Wang, D. Dai, Z. Liu, L. Zheng, Y. Zhang, *J. Mater. Chem. C* **2021**, *9*, 2994.
[5] F. Vatansever, M. R. Hamblin, *Photon. Lasers Med.* **2012**, *1*, 255.
[6] P. Guyot-Sionnest, M. M. Ackerman, X. Tang, *J. Chem. Phys.* **2019**, *151*, 060901.
[7] F. P. García de Arquer, A. Armin, P. Meredith, E. H. Sargent, *Nat. Rev. Mater.* **2017**, *2*, 16100.
[8] F. P. García de Arquer, D. V. Talapin, V. I. Klimov, Y. Arakawa, M. Bayer, E. H. Sargent, *Science* **2021**, *373*, eaaz8541.
[9] Y. Xu, Q. Lin, *Appl. Phys. Rev.* **2020**, *7*, 011315.
[10] Y. Ma, Y. Zhang, W. W. Yu, *J. Mater. Chem. C* **2019**, *7*, 13662.
[11] R. Saran, R. J. Curry, *Nat. Photonics* **2016**, *10*, 81.
[12] I. Moreels, K. Lambert, D. Smeets, D. De Muynck, T. Nollet, J. C. Martins, F. Vanhaecke, A. Vantomme, C. Delerue, G. Allan, Z. Hens, *ACS Nano* **2009**, *3*, 3023.
[13] H. Chen, J. He, S. T. Wu, *IEEE J. Sel. Topics Quantum Electron.* **2017**, *23*, 1900611.
[14] H. Shen, Q. Gao, Y. Zhang, Y. Lin, Q. Lin, Z. Li, L. Chen, Z. Zeng, X. Li, Y. Jia, S. Wang, Z. Du, L. S. Li, Z. Zhang, *Nat. Photon* **2019**, *13*, 192.
[15] Y.-S. Park, J. Roh, B. T. Diroll, R. D. Schaller, V. I. Klimov, *Nat. Rev. Mater.* **2021**, *6*, 382.
[16] H. Lee, H.-J. Song, M. Shim, C. Lee, *Energy Environ. Sci.* **2020**, *13*, 404.
[17] I. L. Medintz, H. T. Uyeda, E. R. Goldman, H. Mattoussi, *Nat. Mater.* **2005**, *4*, 435.
[18] M. A. Boles, D. Ling, T. Hyeon, D. V. Talapin, *Nat. Mater.* **2016**, *15*, 141.
[19] J. W. Lee, D. Y. Kim, F. So, *Adv. Funct. Mater.* **2015**, *25*, 1233.
[20] M. Biondi, M.-J. Choi, Z. Wang, M. Wei, S. Lee, H. Choubisa, L. K. Sagar, B. Sun, S.-W. Baek, B. Chen, P. Todorović, A. M. Najarian, A. Sedighian Rasouli, D.-H. Nam, M. Vafaie, Y. C. Li, K. Bertens, S. Hoogland, O. Voznyy, F. P. García de Arquer, E. H. Sargent, *Adv. Mater.* **2021**, *33*, 2101056.
[21] M. Vafaie, J. Z. Fan, A. Morteza Najarian, O. Ouellette, L. K. Sagar, K. Bertens, B. Sun, F. P. García de Arquer, E. H. Sargent, *Matter* **2021**, *4*, 1042.
[22] M. Liu, O. Voznyy, R. Sabatini, F. P. García de Arquer, R. Munir, A. H. Balawi, X. Lan, F. Fan, G. Walters, A. R. Kirmani, S. Hoogland, F. Laquai, A. Amassian, E. H. Sargent, *Nat. Mater.* **2017**, *16*, 258.
[23] B. O'Regan, M. Grätzel, *Nature* **1991**, *353*, 737.
[24] N. Graddage, J. Ouyang, J. Lu, T.-Y. Chu, Y. Zhang, Z. Li, X. Wu, P. R. L. Malenfant, Y. Tao, *ACS Appl. Nano Mater.* **2020**, *3*, 12209.
[25] J. Ouyang, N. Graddage, J. Lu, Y. Zhong, T.-Y. Chu, Y. Zhang, X. Wu, O. Kodra, Z. Li, Y. Tao, J. Ding, *ACS Appl. Nano Mater.* **2021**, *4*, 13587.
[26] R. Guo, T. Shen, J. Tian, *J. Mater. Chem. C* **2018**, *6*, 2573.
[27] H. Huang, S. Abbaszadeh, *IEEE Sens. J.* **2020**, *20*, 1694.
[28] H. Kannan, J. Stavro, A. Mukherjee, S. Léveillé, K. Kisslinger, L. Guan, W. Zhao, A. Sahu, A. H. Goldan, *ACS Photonics* **2020**, *7*, 1367.
[29] J. R. Scheuermann, A. H. Goldan, O. Tousignant, S. Léveillé, W. Zhao, *Med. Phys.* **2015**, *42*, 1223.
[30] J. R. Scheuermann, A. Howansky, M. Hansroul, S. Léveillé, K. Tanioka, W. Zhao, *Med. Phys.* **2018**, *45*, 794.
[31] S. Kasap, J. B. Frey, G. Belev, O. Tousignant, H. Mani, L. Laperriere, A. Reznik, J. A. Rowlands, *Phys. Status Solidi B* **2009**, *246*, 1794.

[32] A. P. Saunders, *J. Phys. Chem.* **1900**, *4*, 423.
[33] A. Mukherjee, H. Kannan, L. T. Triet Ho, Z. Han, J. Stavro, A. Howansky, N. Nooman, K. Kisslinger, S. Léveillé, O. Kizilkaya, X. Liu, H. Mølnås, S. J. Paul, D. H. Sung, E. Riedo, A. Rumaiz, D. Vasileska, W. Zhao, A. Sahu, A. H. Goldan, *ACS Photonics* **2023**, *10*, 134.
[34] P. R. Brown, D. Kim, R. R. Lunt, N. Zhao, M. G. Bawendi, J. C. Grossman, V. Bulović, *ACS Nano* **2014**, *8*, 5863.
[35] Y. Wang, Z. Liu, N. Huo, F. Li, M. Gu, X. Ling, Y. Zhang, K. Lu, L. Han, H. Fang, A. G. Shulga, Y. Xue, S. Zhou, F. Yang, X. Tang, J. Zheng, M. Antonietta Loi, G. Konstantatos, W. Ma, *Nat. Commun.* **2019**, *10*, 5136.
[36] J. Zhang, R. W. Crisp, J. Gao, D. M. Kroupa, M. C. Beard, J. M. Luther, *J. Phys. Chem. Lett.* **2015**, *6*, 1830.
[37] M. A. Hines, G. D. Scholes, *Adv. Mater.* **2003**, *15*, 1844.
[38] M. Zhu, G. Niu, J. Tang, *J. Mater. Chem. C* **2019**, *7*, 2199.
[39] A. Maier, F. Strauß, P. Kohlschreiber, C. Schedel, K. Braun, M. Scheele, *Nano Lett.* **2022**, *22*, 2809.
[40] J. Liu, P. Liu, D. Chen, T. Shi, X. Qu, L. Chen, T. Wu, J. Ke, K. Xiong, M. Li, H. Song, W. Wei, J. Cao, J. Zhang, L. Gao, J. Tang, *Nat. Electron.* **2022**, *5*, 443.
[41] J. Y. Kim, V. Adinolfi, B. R. Sutherland, O. Voznyy, S. J. Kwon, T. W. Kim, J. Kim, H. Ihee, K. Kemp, M. Adachi, M. Yuan, I. Kramer, D. Zhitomirsky, S. Hoogland, E. H. Sargent, *Nat. Commun.* **2015**, *6*, 7772.
[42] R. Dong, C. Bi, Q. Dong, F. Guo, Y. Yuan, Y. Fang, Z. Xiao, J. Huang, *Adv. Opt. Mater.* **2014**, *2*, 549.
[43] J. R. Manders, T.-H. Lai, Y. An, W. Xu, J. Lee, D. Y. Kim, G. Bosman, F. So, *Adv. Funct. Mater.* **2014**, *24*, 7205.
[44] R. Sliz, M. Lejay, J. Z. Fan, M.-J. Choi, S. Kinge, S. Hoogland, T. Fabritius, F. P. García de Arquer, E. H. Sargent, *ACS Nano* **2019**, *13*, 11988.
[45] B. N. Pal, I. Robel, A. Mohite, R. Laocharoensuk, D. J. Werder, V. I. Klimov, *Adv. Funct. Mater.* **2012**, *22*, 1741.
[46] S. Lu, P. Liu, J. Yang, S. Liu, Y. Yang, L. Chen, J. Liu, Y. Liu, B. Wang, X. Lan, J. Zhang, L. Gao, J. Tang, *ACS Appl. Mater. Interfaces* **2023**, *15*, 12061.
[47] O. Atan, J. M. Pina, D. H. Parmar, P. Xia, Y. Zhang, A. Gulsaran, E. D. Jung, D. Choi, M. Imran, M. Yavuz, S. Hoogland, E. H. Sargent, *Nano Lett.* **2023**, *23*, 4298.
[48] J. P. Clifford, G. Konstantatos, K. W. Johnston, S. Hoogland, L. Levina, E. H. Sargent, *Nat. Nanotechnol.* **2009**, *4*, 40.
[49] A. Rogalski, J. Antoszewski, L. Faraone, *J. Appl. Phys.* **2009**, *105*, 091101.
[50] W.-D. Park, K. Tanioka, *Appl. Phys. Lett.* **2014**, *105*, 192106.
[51] C.-H. M. Chuang, P. R. Brown, V. Bulović, M. G. Bawendi, *Nat. Mater.* **2014**, *13*, 796.
[52] J. Qu, N. Goubet, C. Livache, B. Martinez, D. Amelot, C. Gréboval, A. Chu, J. Ramade, H. Cruguel, S. Ithurria, M. G. Silly, E. Lhuillier, *J. Phys. Chem. C* **2018**, *122*, 18161.
[53] Y. Liu, F. Li, G. Shi, Z. Liu, X. Lin, Y. Shi, Y. Chen, X. Meng, Y. Lv, W. Deng, X. Pan, W. Ma, *ACS Energy Lett.* **2020**, *5*, 3797.
[54] A. Chu, B. Martinez, S. Ferré, V. Noguier, C. Gréboval, C. Livache, J. Qu, Y. Prado, N. Casaretto, N. Goubet, H. Cruguel, L. Dudy, M. G. Silly, G. Vincent, E. Lhuillier, *ACS Appl. Mater. Interfaces* **2019**, *11*, 33116.
[55] A. Jagtap, B. Martinez, N. Goubet, A. Chu, C. Livache, C. Gréboval, J. Ramade, D. Amelot, P. Trousset, A. Triboulin, S. Ithurria, M. G. Silly, B. Dubertret, E. Lhuillier, *ACS Photonics* **2018**, *5*, 4569.
[56] E. L. Runnerstrom, G. K. Ong, G. Gregori, J. Maier, D. J. Milliron, *J. Phys. Chem. C* **2018**, *122*, 13624.
[57] M.-W. Kim, Y. Yuan, S. Jeong, J. Chong, H. Mølnås, A. Alaei, I. J. Cleveland, N. Liu, Y. Ma, S. Strauf, E. S. Aydil, A. Sahu, D. M. Kalyon, S. S. Lee, *Adv. Funct. Mater.* **2022**, *32*, 2207326.